International Journal of Computational Fluid Dynamics

ISSN: 1061-8562 (Print) 1029-0257 (Online) Journal homepage: www.tandfonline.com/journals/gcfd20

Aerodynamic shape optimization for unsteady three-dimensional flows

Siva K. Nadarajah, Matthew S. McMullen & Antony Jameson

To cite this article: Siva K. Nadarajah, Matthew S. McMullen & Antony Jameson (2006) Aerodynamic shape optimization for unsteady three-dimensional flows, International Journal of Computational Fluid Dynamics, 20:8, 533-548, DOI: 10.1080/10618560601088343

To link to this article: https://doi.org/10.1080/10618560601088343

Published online: 14 Feb 2007.

International Journal of Computational Fluid Dynamics, Vol. 20, No. 8, September 2006, 533–548

Taylor & Francis
Taylor & Francis Group

Aerodynamic shape optimization for unsteady three-dimensional flows

SIVA K. NADARAJAH†¶*, MATTHEW S. MCMULLEN‡§ and ANTONY JAMESON‡‖

†CFD Lab, Department of Mechanical Engineering, McGill University, 688 Sherbrooke Street West, Room 711, Montreal, Que., Canada H3A 2S6
‡Department of Aeronautics and Astronautics, Stanford University, Durand Building, 496 Lomita Mall, Stanford, CA 94305, USA

(Received 29 April 2005; in final form 11 July 2006)

This paper presents an adjoint method for the optimum shape design of unsteady flows. The goal is to develop a set of discrete unsteady adjoint equations and the corresponding boundary condition for the non-linear frequency domain method. First, this paper presents the complete formulation of the time dependent optimal design problem. Second, we present the non-linear frequency domain adjoint equations for three-dimensional flows. Third, we present results that demonstrate the application of the theory to a three-dimensional wing.

Keywords: Adjoint method; Optimization; Unsteady flow; Frequency domain; Computational fluid dynamics

1. Introduction

There are numerous important engineering applications in which the flow is inherently unsteady but periodic. Helicopter rotors in forward flight, turbomachinery blades and cooling fans operate in unsteady flow and are constantly subjected to unsteady loads. Optimization techniques for unsteady flows are clearly needed to improve their performance and to alleviate the unsteady effects that contribute to flutter, buffeting, poor gust and acoustic response and dynamic stall. As yet there have been few efforts in this direction.

One of the major reasons for this is the demanding computational cost associated with the calculation of unsteady flows. As part of the accelerated strategic computing initiative (ASCI) project at Stanford, Davis (2001) presented estimates for the computational cost of a multistage compressor and turbine calculation based on the parallel execution of 750 processors operating 8 h a day. He concluded that it would require 1300 days to compute the flow through a 23 blade row compressor. The overwhelming majority of the computational time is spent on time accurately resolving the decay of the initial transients. Although this example is an extreme case, it illustrates the prohibitive cost of many unsteady calculations using time accurate solvers to find a periodic steady state.

Nevertheless, the development of optimum shape design for two-dimensional unsteady flows using the time accurate adjoint based design approach has been pursued by Nadarajah and Jameson (2002) and Nadarajah (2003). Their work is largely based on algorithms developed for aerodynamic shape optimization (ASO) for a steady flow environment (Jameson 1989, 1995, Reuther *et al.* 1996a,b, Nadarajah *et al.* 2002). Nadarajah derived and applied the time accurate adjoint equations (both the continuous and discrete) to the redesign of an oscillating airfoil in an inviscid transonic flow. The redesigned shape achieved a reduction in the time-averaged drag while maintaining the time-averaged lift. The approach utilized a dual time stepping (Jameson 1991) technique that implements a fully implicit second order backward difference formula to discretize the time derivative. Typical runs required 15 periods with 24 discrete time steps per period and 15 multigrid cycles at each time step. Encouraging results were obtained at a substantial computational expense.

The prohibitive cost of computing three-dimensional unsteady flows using the time accurate approach has motivated a new interest in using periodic methods.

*Corresponding author. Tel.: + 1-514-398-5757. Email: siva.nadarajah@mcgill.ca
¶Assistant Professor, McGill University.
§Post-Doctoral Fellow.
‖Thomas V. Jones, Professor of Engineering, Stanford University, AIAA Fellow.

International Journal of Computational Fluid Dynamics
ISSN 1061-8562 print/ISSN 1029-0257 online © 2006 Taylor & Francis
http://www.tandf.co.uk/journals
DOI: 10.1080/10618560601088343

Linearized frequency domain and deterministic-stress (Adamczyk 1984) methods are examples of periodic methods. However, these methods generally do not account for strong non-linearities in the system. Pseudo-spectral approaches in space and time have been implemented for a multitude of non-linear problems throughout the numerical analysis literature. The harmonic balance technique proposed by Hall (2000) and Hall *et al.* (2000) represents the first pseudo-spectral method in time for the unsteady Euler equations. The non-linear frequency domain method (NLFD) proposed by McMullen *et al.* (2001, 2002) is a similar approach that was later validated for the unsteady Navier–Stokes equations. These approaches are spectral techniques which converge at an exponential rate to the exact solution, even in the presence of aliasing affects (Snider 1972). This can be compared to more classical finite difference schemes, which contain errors proportional to some power of the grid spacing. An analysis presented in McMullen's (2003) thesis demonstrates the comparative advantage of spectral techniques for real world applications. Using an unsteady pitching airfoil in a transonic flow, he calculated the error in the magnitude of the fundamental harmonic for the coefficient of lift. The data showed that an NLFD calculation employing one time varying harmonic (which can be represented with three discrete samples) produced an error level equivalent to that of a time accurate calculation using 45 time steps per period. For this case, the NLFD calculation was roughly an order of magnitude more efficient than time accurate codes operating at equivalent error levels.

Recently, there have been two investigations into the modeling of unsteady aerodynamic design sensitivities. Duta *et al.* (2002) have presented a harmonic adjoint approach for unsteady turbomachinery design. The aim of the work was to reduce blade vibrations due to flow unsteadiness. The research produced adjoint methods that were based on a linearized analysis of periodic unsteady flows. Thomas *et al.* (2003) presented a viscous discrete adjoint approach for computing unsteady aerodynamic design sensitivities. The adjoint code was generated from the harmonic balance flow solver with the use of an automatic differentiation software compiler.

The motivation of the research in this paper has been fueled both by the success of our current capability for automatic shape optimization for unsteady flows and the future potential of the NLFD method. The general goal of this work is to extend the NLFD method for adjoint based design approach from two-dimensional (Nadarajah *et al.* 2003) to three-dimensional flows. The result of this effort is a NLFD adjoint design code that is fully non-linear and the computational cost of the adjoint module is proportional to the cost of the flow solver.

2. Governing equations

In order to allow for geometric shape changes, it is convenient to use a body fitted coordinate system, so that the computational domain is fixed. This requires the formulation of the Euler equations in the transformed coordinate system. Einstein notation simplifies the presentation of the equations, where summation over $i = 1–3$ is implied by a repeated index i. Then the three-dimensional compressible Euler equations for a rigidly translating control volume may be written as

$$\frac{\partial w}{\partial t} + \frac{\partial f_i}{\partial x_i} = 0 \text{ in } D,$$

where

$$w = \begin{Bmatrix} \rho \\ \rho u_1 \\ \rho u_2 \\ \rho u_3 \\ \rho E \end{Bmatrix}, \quad f_i = \begin{Bmatrix} \rho (u_i - x_{t_i}) \\ \rho u_1 (u_i - x_{t_i}) + p\delta_{i1} \\ \rho u_2 (u_i - x_{t_i}) + p\delta_{i2} \\ \rho u_3 (u_i - x_{t_i}) + p\delta_{i3} \\ \rho E (u_i - x_{t_i}) + p u_i \end{Bmatrix}.$$

In these equations, ρ is the density, x_i are the Cartesian coordinates, u_i, x_{t_i} are the Cartesian velocity components of the fluid and boundary, respectively, E is the total energy and δ_{ij} is the Kronecker delta function. The results presented in this paper are based on transonic flow calculations where the ideal gas equation is applicable. Consequently, the pressure, p, can be expressed as

$$p = (\gamma - 1)\rho \left\{ E - \frac{1}{2}\left(u_i^2\right) \right\},$$

and $\rho H = \rho E + p$, where γ is the ratio of the specific heats.

Consider a transformation to coordinates ξ_1, ξ_2, ξ_3 where

$$K_{ij} = \left[\frac{\partial x_i}{\partial \xi_j}\right], \quad J = \det(K), \quad K_{ij}^{-1} = \left[\frac{\partial \xi_i}{\partial x_j}\right],$$

and $S = JK^{-1}$. The elements of S are the coefficients of K and in a finite volume discretization, they are just the face areas of the computational cells projected in the x_1, x_2 and x_3 directions. Also introduce scaled contravariant velocity components as

$$U_i = S_{ij} u_j, \quad \text{and} \quad X_{t_i} = S_{ij} x_{t_j}.$$

The Euler equations can now be written as

$$\frac{\partial (Jw)}{\partial t} + \frac{\partial F_i}{\partial \xi_i} = 0 \text{ in } D, \tag{1}$$

where

$$F_i = S_{ij} f_j = \begin{bmatrix} \rho\left(U_i - X_{t_i}\right) \\ \rho u_1 \left(U_i - X_{t_i}\right) + S_{j1} p \\ \rho u_2 \left(U_i - X_{t_i}\right) + S_{j2} p \\ \rho u_3 \left(U_i - X_{t_i}\right) + S_{j3} p \\ \rho E \left(U_i - X_{t_i}\right) + p U_i \end{bmatrix}.$$

Assume now that the new computational coordinate system conforms to the wing in such a way that the wing surface $\mathcal{B}_W$ is represented by $\xi_2 = 0$. Then the flow is determined as the steady state solution of equation (1)

subject to the flow tangency condition

$$U_2 = 0 \quad \text{on} \quad \mathcal{B}_{\mathrm{W}}.$$

At the far field boundary $\mathcal{B}_{\mathrm{FF}}$, conditions are specified for incoming waves, as in the two-dimensional case, while outgoing waves are determined by the solution.

The simulations contained in this research are restricted to rigid mesh translation. Consequently, the volumetric integral can be approximated as the product of the cell volume and the temporal derivative of the solution at the cell center. In semi-discrete form, equation (1) can be written as

$$V\frac{\partial w}{\partial t} + R(w) = 0. \tag{2}$$

To eliminate odd–even decoupling of the solution and overshoots before and after shock waves, the convective flux is added to a diffusion flux. The artificial dissipation scheme used in this research is a blended first and third order flux, first introduced by Jameson *et al.* (1981). The artificial dissipation scheme is defined as,

$$d = \epsilon^{(2)}\Delta x^3 \frac{\lambda}{p}\left|\frac{\partial^2 p}{\partial x^2}\right|\frac{\partial w}{\partial x} - \epsilon^{(4)}\Delta x^3 \lambda \frac{\partial^3 w}{\partial x^3}. \tag{3}$$

The first term in equation (3) is a first order scalar diffusion term, where the magnitude of the term is scaled by the normalized second difference of the pressure and serves to damp oscillations around shock waves. $\epsilon^{(4)}$ is the coefficient for the third derivative of the artificial dissipation flux. The coefficient is scaled such that it is zero at regions of large gradients, such as shock waves and eliminates odd–even decoupling elsewhere.

2.1. Numerical discretization

A finite-volume methodology is used to discretize the integral form of the conservation laws. When equation (1) is formulated for each computational cell, a system of first order ordinary differential equations is obtained. The convective flux is represented in discrete form for each computational cell using a central second-order discretization. Equation (1) can then be written for each computational cell as

$$V\frac{\partial w_{i,j,k}}{\partial t} + R(w)_{i,j,k} = 0. \tag{4}$$

The residual can then be represented as

$$R(w)_{i,j,k} = h_{i+(1/2),j,k} - h_{i-(1/2),j,k} + h_{i,j+(1/2),k} - h_{i,j-(1/2),k} + h_{i,j,k+(1/2)} - h_{i,j,k-(1/2)}, \tag{5}$$

where $h_{i+(1/2),j,k} = F_{i+(1/2),j,k} - D_{i+(1/2),j,k}$ and D represents the artificial dissipation term. The $\pm(1/2)$ notation indicates that the quantity is calculated at the flux faces.

The values of the flow variables are stored at the cell centers and can be regarded as cell averages. Accordingly, the convective flux $F_{i+(1/2),j,k}$ at the cell face as shown in figure 1, is computed by taking the average of the flux contributions from each cell across the cell face as shown

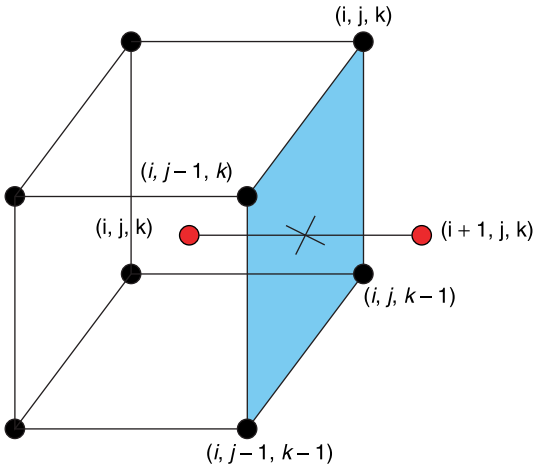

Figure 1. Finite volume mesh for cell (i,j,k).

in the following equation

$$F_{i+(1/2),j,k} = \frac{1}{2}\left(F^{+}_{i+1,j,k} + F^{-}_{i,j,k}\right).$$

Next we define the flux velocities asab

$$q^{-} = \frac{1}{\rho_{i,j,k}}\Big(S_{11_{i+(1/2),j,k}}(\rho u_1)_{i,j,k} + S_{12_{i+(1/2),j,k}}(\rho u_2)_{i,j,k} + S_{13_{i+(1/2),j,k}}(\rho u_3)_{i,j,k}\Big),$$

and

$$q^{+} = \frac{1}{\rho_{i,j,k}}\Big(S_{11_{i+(1/2),j,k}}(\rho u_1)_{i+1,j,k} + S_{12_{i+(1/2),j,k}}(\rho u_2)_{i+1,j,k} + S_{13_{i+(1/2),j,k}}(\rho u_3)_{i+1,j,k}\Big).$$

The mesh flux velocity is computed as follows

$$q_{x_t} = S_{11_{i+(1/2),j,k}}(x_{t_1})_{i,j,k} + S_{12_{i+(1/2),j,k}}(x_{t_2})_{i,j,k} + S_{13_{i+(1/2),j,k}}(x_{t_3})_{i,j,k}.$$

Then the flux vectors can be formulated as

$$F^{+}_{i+1,j,k} = \left\{\begin{array}{l} \rho_{i+1,j,k}\left(q^{+} - q_{x_t}\right) \\ (\rho u_1)_{i+1,j,k}\left(q^{+} - q_{x_t}\right) + S_{11_{i+(1/2),j,k}}p_{i+1,j,k} \\ (\rho u_2)_{i+1,j,k}\left(q^{+} - q_{x_t}\right) + S_{12_{i+(1/2),j,k}}p_{i+1,j,k} \\ (\rho u_3)_{i+1,j,k}\left(q^{+} - q_{x_t}\right) + S_{13_{i+(1/2),j,k}}p_{i+1,j,k} \\ (\rho E)_{i+1,j,k}\left(q^{+} - q_{x_t}\right) + p_{i+1,j,k}q^{+} \end{array}\right\},$$

and

$$F^{-}_{i,j,k} = \left\{\begin{array}{l} \rho_{i,j,k}\left(q^{-} - q_{x_t}\right) \\ (\rho u_1)_{i,j,k}\left(q^{-} - q_{x_t}\right) + S_{11_{i+(1/2),j,k}}p_{i,j,k} \\ (\rho u_2)_{i,j,k}\left(q^{-} - q_{x_t}\right) + S_{12_{i+(1/2),j,k}}p_{i,j,k} \\ (\rho u_3)_{i,j,k}\left(q^{-} - q_{x_t}\right) + S_{13_{i+(1/2),j,k}}p_{i,j,k} \\ (\rho E)_{i,j,k}\left(q^{-} - q_{x_t}\right) + p_{i,j,k}q^{-} \end{array}\right\}.$$

The blended first-and third-order artificial dissipation term as defined in equation (3) is discretized as

$$D_{i+(1/2),j,k} = \nu^{(2)}_{i+(1/2),j,k}\Lambda_{i+(1/2),j,k}\Delta_{i+(1/2),j,k} - \nu^{(4)}_{i+(1/2),j,k}\Lambda_{i+(1/2),j,k}\left[\Delta_{i+(3/2),j,k} - 2\Delta_{i+(1/2),j,k} + \Delta_{i-(1/2),j,k}\right].$$

where $\Delta_{i+(1/2),j,k} = w_{i+1,j,k} - w_{i,j,k}$. The coefficients $\nu^{(2)}$ and $\nu^{(4)}$ are the products of the adjustable constants and the normalized second difference of the pressure. $\Lambda_{i+(1/2),j,k}$ is the rescaled numerical spectral radius of the flux Jacobian matrix and directionally scales the dissipative terms.

The residual $R(w)_{i,j,k}$ is then formed by adding contributions from the convective and dissipative fluxes. A modified five stage Runge-Kutta time integration scheme is then introduced to march the solution to a steady state solution. Local time stepping, residual averaging, and multigrid are employed to accelerate the convergence.

3. Formulation of the time-dependent optimal design problem

Optimal control of time dependent trajectories is generally complicated by the need to solve the adjoint equation in reverse time from a final boundary condition using data from the trajectory solution, which in turn depends on the control derived from the adjoint solution.

Introduce the cost function

$$I = \int_0^{t_f} \mathcal{L}(w,f)\,\mathrm{d}t + \mathcal{M}(w(t_f)),$$

where the function $\mathcal{L}$ depends on the flow solution w and the shape function f and the function $\mathcal{M}$ depends on the time dependent flow solution. Assume that the following equation defines the time-dependent flow solution

$$V\frac{\partial w}{\partial t} + R(w,f) = 0,$$

where V is the cell volume and R represents a residue containing the convective and dissipative fluxes. A change in f results in a change

$$\delta I = \int_0^{t_f}\left(\frac{\partial \mathcal{L}^{\mathrm{T}}}{\partial w}\delta w + \frac{\partial \mathcal{L}^{\mathrm{T}}}{\partial f}\delta f\right)\mathrm{d}t + \frac{\partial \mathcal{M}^{\mathrm{T}}}{\partial w}\delta w(t_f),$$

in the cost function. The variation in the flow solution is

$$V\frac{\partial}{\partial t}\delta w + \frac{\partial R}{\partial w}\delta w + \frac{\partial R}{\partial f}\delta f = 0.$$

Next, introduce a Lagrange multiplier ψ to the time-dependent flow equation, integrate it over time and subtract it from the variation of the cost function to arrive at the following equation.

$$\delta I = \int_0^{t_f}\left(\frac{\partial \mathcal{L}^{\mathrm{T}}}{\partial w}\delta w + \frac{\partial \mathcal{L}^{\mathrm{T}}}{\partial f}\delta f\right)\mathrm{d}t + \frac{\partial \mathcal{M}^{\mathrm{T}}}{\partial w}\delta w(t_f) - \int_0^{t_f}\psi^{\mathrm{T}}\left(V\frac{\partial}{\partial t}\delta w + \frac{\partial R}{\partial w}\delta w + \frac{\partial R}{\partial f}\delta f\right)\mathrm{d}t.$$

By integrating the term $\int_0^{t_f}\psi^{\mathrm{T}}V(\partial/\partial t)\delta w\,\mathrm{d}t$ by parts, yields

$$\delta I = \int_0^{t_f}\left(\frac{\partial \mathcal{L}^{\mathrm{T}}}{\partial w} + V\frac{\partial \psi^{\mathrm{T}}}{\partial t} - \psi^{\mathrm{T}}\frac{\partial R}{\partial w}\right)\delta w\,\mathrm{d}t + \left(\frac{\partial \mathcal{M}^{\mathrm{T}}}{\partial w} - \psi^{\mathrm{T}}(t_f)\right)\delta w(t_f) + \int_0^{t_f}\left(\frac{\partial \mathcal{L}^{\mathrm{T}}}{\partial f} - \psi^{\mathrm{T}}\frac{\partial R}{\partial f}\right)\delta f\,\mathrm{d}t.$$

Choose ψ to satisfy the adjoint equation

$$V\frac{\partial \psi}{\partial t} = \left(\frac{\partial R}{\partial w}\right)^{\mathrm{T}}\psi - \left(\frac{\partial \mathcal{L}}{\partial w}\right)$$

with the terminal boundary condition

$$\psi(t_f) = \frac{\partial \mathcal{M}}{\partial w}.$$

Then

$$\delta I = \mathcal{G}^{\mathrm{T}}\delta f,$$

where

$$\mathcal{G}^{\mathrm{T}} = \int_0^{t_f}\left(\frac{\partial \mathcal{L}^{\mathrm{T}}}{\partial f} - \psi^{\mathrm{T}}\frac{\partial R}{\partial f}\right)\mathrm{d}t.$$

The sensitivity derivatives are determined by the solution of the adjoint equation in reverse time from the terminal boundary condition and the time-dependent solution of the flow equation. These sensitivity derivatives are then used to get a direction of improvement and steps are taken until convergence is achieved.

The computational costs of unsteady optimization problems are directly proportional to the desired number of time steps. The unsteady flow calculation can be obtained either by the use of implicit time-stepping schemes or a NLFD approach.

4. Description of the UFSYN88-MBC multiblock code

The development of a multiblock code for the design method entails three separate parts: the solution of the flow equations, the solution of the adjoint equations and the calculation of the gradient integral formulas. Both the flow and adjoint solutions are obtained using a finite volume discretization of the governing equations with the flow and adjoint variables stored at cell centers. Similarities between the flow and adjoint equations allow them to be solved using exactly the same efficient numerical scheme, with the exception of the boundary conditions; where

in the case of the adjoint equation, the boundary condition appears as source terms and are added to the adjoint fluxes. Therefore, the same domain decomposition is used for the flow and adjoint solvers.

The three-dimensional C–H meshes for the wing were generated using a conformal mapping transformation method. Flows were computed on $n_i \times n_j \times n_k = 193 \times 33 \times 97$ mesh. The domain was decomposed into sub-domains containing $(n_i/N_{p_i}) \times (n_j/N_{p_j}) \times (n_k/N_{p_k})$ points, where N_{p_i}, N_{p_j} and N_{p_k} are the number of sub-domains in the i,j and k coordinate directions. The number of sub-domains in each coordinate direction is an input into the program. It must also be mentioned that the number of sub-domains in each coordinate direction limits the number of maximum number of multigrid levels that can be used. This limits the convergence rate of the multiblock code. Domains were decomposed such that at least four multigrid levels were possible in each sub-domain. Communication between sub-domains is performed through halo cells surrounding each sub-domain boundary. Since both the convective and dissipative fluxes are calculated at the cell faces, all six neighboring cells are needed to compute the convective flux through the face and twelve cells are needed for the dissipative flux which uses blended first- and third-order differences.

5. Development of the non-linear frequency domain adjoint equations

The derivation of the NLFD method starts with the semi-discrete form of the governing equations, and assumes that the solution w and spatial operator R can be represented by separate Fourier series:

$$w = \sum_{k=-(N/2)}^{(N/2)-1} \hat{w}_k \, \mathrm{e}^{ikt}, \quad R = \sum_{k=-(N/2)}^{(N/2)-1} \hat{R}_k \, \mathrm{e}^{ikt} \tag{6}$$

where,

$$i = \sqrt{-1}. \tag{7}$$

Here, however each coefficient $\hat{R}_k$ of the transform of the residual depends on all the coefficients $\hat{w}_k$, because $R(w(t))$ is a non-linear function of $w(t)$. Thus equation (8) represents a non-linear set of equations which must be iteratively solved. The solver attempts to find a solution, w, that drives this system of equations to zero for all wavenumbers, but at any iteration in the solution process the unsteady residual, R^*, will be finite:

$$\hat{R}_k^* = ikV\hat{w}_k + \hat{R}_k. \tag{8}$$

The nonlinearity of the unsteady residual stems from the spatial operator. There are two approaches to calculating the spatial operator expressed in the frequency domain. The first uses a complex series of convolution sums to calculate $\hat{R}_k$ directly from $\hat{w}_k$. This approach is discarded due to its massive complexity (considering artificial dissipation schemes and turbulence modeling) and cost that scales quadratically with the number of modes N. Instead, we implement a pseudo-spectral approach in time. This approach requires several transformations between the physical and frequency domains which are performed by a fast Fourier transform (FFT). The computational cost of this transform scales like $N \log(N)$, where N is a large number. A diagram detailing the transformations used by the pseudo spectral approach is provided in figure 2.

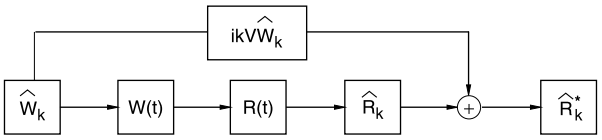

Figure 2. Simplified dataflow diagram of the time advancement scheme illustrating the pseudo-spectral approach used in calculating the non-linear spatial operator R.

The pseudo-spectral approach begins by assuming that $\hat{w}_k$ is known for all wavenumbers. Using an inverse FFT, $\hat{w}_k$ can be transformed back to the physical space resulting in a state vector $w(t)$ sampled at evenly distributed intervals over the time period. At each of these time instances, the steady-state operator $R(w(t))$ can be computed. A FFT is then used to transform the spatial operator to the frequency domain where $\hat{R}_k$ is known for all wavenumbers. The unsteady residual $\hat{R}_k^*$ can then be calculated by adding $\hat{R}_k$ to the spectral representation of the temporal derivative $ikV\hat{w}_k$.

Consistent with the time accurate approach, a pseudo-time derivative can be added and a time-stepping scheme can be employed to numerically integrate the resulting equations.

$$V\frac{\partial \hat{w}_k}{\partial \tau} + \hat{R}_k^* = 0. \tag{9}$$

In the NLFD case, an unsteady residual exists for each wavenumber used in the solution and the pseudo-time derivative acts as a gradient to drive the absolute value of all of these components to zero simultaneously.

The NLFD discrete adjoint equation can be developed using two separate approaches. In the first approach, we first take a variation of the unsteady residual $\hat{R}_k^*$ represented in equation (8) with respect to the state vector $\hat{w}_k$ and shape function f, to produce

$$\delta\hat{R}_k^* = ikV\delta\hat{w}_k + \delta\hat{R}_k.$$

The next step would be to expand $\delta\hat{R}_k$ as a function of $\hat{w}_k$. As mentioned earlier, this approach would require a series of convolution sums to express $\delta\hat{R}_k$ as a function of $\delta\hat{w}_k$. This method was not implemented due to its computational cost and added complexity. Instead, the adjoint equations were solved using a pseudo-spectral approach similar to the one applied to the flow equations.

In the latter approach, the NLFD adjoint equations are developed from the semi-discrete from of the adjoint

equation, which can be as expressed as

$$V\frac{\partial \psi}{\partial t} + R(\psi) = 0,$$

where $R(\psi)$ is the sum of all the spatial operators, both convective and dissipative, used in the discretized adjoint equations. Refer to Nadarajah (2003) for a detailed derivation of these spatial operators and boundary conditions. Next, we assume that the adjoint variable and spatial operator can be expressed as a Fourier series:

$$\psi = \sum_{k=-(N/2)}^{(N/2)-1} \hat{\psi}_k \, \mathrm{e}^{ikt}, \quad R(\psi) = \sum_{k=-(N/2)}^{(N/2)-1} \widehat{R(\psi)}_k \, \mathrm{e}^{ikt}. \quad (10)$$

The derivation of the NLFD adjoint then follows that of the NLFD flow equations. The NLFD adjoint equations are expressed as

$$V\frac{\partial \hat{\psi}_k}{\partial \tau} + \widehat{R(\psi)}^*_k = 0.$$

where $\widehat{R(\psi)}^*_k = ikV\hat{\psi}_k + \widehat{R(\psi)}_k$. The pseudo-spectral approach illustrated in figure 2 is employed in the NLFD adjoint code to form the unsteady residual. This term in conjunction with a pseudo time derivative provides an iterative solution process consistent with that documented for the flow equations.

5.1. Numerical discretization

The discrete adjoint equation is obtained by applying control theory directly to the set of discrete field equations. To formulate the discrete adjoint equation, we first define the cost function I as such,

$$I = C_D,$$

where C_D is total wing drag coefficient, p is the current near field pressure and p_{T} is the target near field pressure. Next, we take a variation of the residual term, which can be written as

$$\begin{aligned}\delta R(w)_{i,j,k} = {} & \delta h_{i+(1/2),j,k} - \delta h_{i-(1/2),j,k} \\ & + \delta h_{i,j+(1/2),k} - \delta h_{i,j-(1/2),k} \\ & + \delta h_{i,j,k+(1/2)} - \delta h_{i,j,k-(1/2)}, \end{aligned} \quad (11)$$

with $\delta h_{i+(1/2),j,k} = \delta F_{i+(1/2),j,k} - \delta D_{i+(1/2),j,k}$. We then pre-multiply the variation of the discrete residual by the transpose of the Lagrange multiplier and sum the product over the computational domain to produce the following

$$\sum_{i=2}^{i_{\max}} \sum_{j=2}^{j_{\max}} \sum_{k=2}^{k_{\max}} \psi^{\mathrm{T}}_{i,j,k} \delta R(w)_{i,j,k}.$$

The variation of the cost function, δI, can then be augmented by the product of the variation of the discrete governing equation and the Lagrange multiplier $\psi^{\mathrm{T}}_{i,j,k}$

$$\delta I = \delta C_D + \sum_{i=2}^{i_{\max}} \sum_{j=2}^{j_{\max}} \sum_{k=2}^{k_{\max}} \psi^{\mathrm{T}}_{i,j,k} \delta R(w)_{i,j,k}. \quad (12)$$

In order to eliminate δw from equation (12), terms multiplied by the variation $\delta w_{i,j,k}$ of the discrete flow variables are collected and equated to zero. The following is the resulting discrete adjoint equation,

$$\begin{aligned} V\frac{\partial \psi_{i,j}}{\partial t} = \frac{1}{2}\Big[& \Big(S_{11_{i-(1/2),j,k}} A^{\mathrm{T}}_{1_{i,j,k}} + S_{12_{i-(1/2),j,k}} A^{\mathrm{T}}_{2_{i,j,k}} \\ & + S_{13_{i-(1/2),j,k}} A^{\mathrm{T}}_{3_{i,j,k}}\Big)(\psi_{i,j,k} - \psi_{i-1,j,k}) \\ & + \Big(S_{11_{i+(1/2),j,k}} A^{\mathrm{T}}_{1_{i,j,k}} + S_{12_{i+(1/2),j,k}} A^{\mathrm{T}}_{2_{i,j,k}} \\ & + S_{13_{i+(1/2),j,k}} A^{\mathrm{T}}_{3_{i,j,k}}\Big)(\psi_{i+1,j,k} - \psi_{i,j,k}) \\ & + \Big(S_{21_{i,j+(1/2),k}} A^{\mathrm{T}}_{1_{i,j,k}} + S_{22_{i,j+(1/2),k}} A^{\mathrm{T}}_{2_{i,j,k}} \\ & + S_{23_{i,j+(1/2),k}} A^{\mathrm{T}}_{3_{i,j,k}}\Big)(\psi_{i,j+1,k} - \psi_{i,j,k}) \\ & + \Big(S_{21_{i,j-(1/2),k}} A^{\mathrm{T}}_{1_{i,j,k}} + S_{22_{i,j-(1/2),k}} A^{\mathrm{T}}_{2_{i,j,k}} \\ & + S_{23_{i,j-(1/2),k}} A^{\mathrm{T}}_{3_{i,j,k}}\Big)(\psi_{i,j,k} - \psi_{i,j-1,k}) \\ & + \Big(S_{31_{i,j,k+(1/2)}} A^{\mathrm{T}}_{1_{i,j,k}} + S_{32_{i,j,k+(1/2)}} A^{\mathrm{T}}_{2_{i,j,k}} \\ & + S_{33_{i,j,k+(1/2)}} A^{\mathrm{T}}_{3_{i,j,k}}\Big)(\psi_{i,j,k+1} - \psi_{i,j,k}) \\ & + \Big(S_{31_{i,j,k-(1/2)}} A^{\mathrm{T}}_{1_{i,j,k}} + S_{32_{i,j,k-(1/2)}} A^{\mathrm{T}}_{2_{i,j,k}} \\ & + S_{33_{i,j,k-(1/2)}} A^{\mathrm{T}}_{3_{i,j,k}}\Big)(\psi_{i,j,k} - \psi_{i,j,k-1})\Big] \\ & + \mathcal{D}_{i+(1/2),j,k} - \mathcal{D}_{i-(1/2),j,k} + \mathcal{D}_{i,j+(1/2),k} \\ & - \mathcal{D}_{i,j-(1/2),k} + \mathcal{D}_{i,j,k+(1/2)} - \mathcal{D}_{i,j,k-(1/2)}. \end{aligned} \quad (13)$$

where A^{T} is the transpose of the convective flux Jacobian $\partial f/\partial w$, V is the cell area and

$$\begin{aligned} \mathcal{D}_{i+(1/2),j,k} = {} & \nu^{(2)}_{i+(1/2),j,k} \Lambda_{i+(1/2),j,k} \Big(\psi^{\mathrm{T}}_{i+1,j,k} - \psi^{\mathrm{T}}_{i,j,k}\Big) \\ & - \nu^{(4)}_{i+(3/2),j,k} \Lambda_{i+(3/2),j,k} \Big(\psi^{\mathrm{T}}_{i+2,j,k} - \psi^{\mathrm{T}}_{i+1,j,k}\Big) \\ & + 2\nu^{(4)}_{i+(1/2),j,k} \Lambda_{i+(1/2),j,k} \Big(\psi^{\mathrm{T}}_{i+1,j,k} - \psi^{\mathrm{T}}_{i,j,k}\Big) \\ & - \nu^{(4)}_{i-(1/2),j,k} \Lambda_{i-(1/2),j,k} \Big(\psi^{\mathrm{T}}_{i,j,k} - \psi^{\mathrm{T}}_{i-1,j,k}\Big), \end{aligned}$$

is the discrete adjoint artificial dissipation term which corresponds to the discretization of the inviscid flow equations by the Jameson–Schmidt–Turkel (1981) (JST) scheme. The dissipation coefficients $\nu^{(2)}$ and $\nu^{(4)}$ are functions of the flow variables, but, in order to reduce complexity, they are treated as constants. The effect of this partial discretization has been explored by Nadarajah and Jameson (2000, 2001).

6. Optimization procedure

In this paper, the inverse design boundary condition is applied to the near field, while sensitivity derivatives or the gradient are calculated on the airfoil surface. The gradient for the discrete adjoint is obtained by perturbing each point on the lower wall. Once the gradient $\mathcal{G}$ has been determined, it can be used to drive a variety of gradient-based search procedures. The search procedure used in this work is a descent method in which small steps are taken in the negative gradient direction. Let $\mathcal{F}$ represent the design variable and $\mathcal{G}$ the gradient. Then an improvement can be made with a shape change

$$\delta\mathcal{F} = -\lambda\mathcal{G}.$$

However, it is better to replace the gradient $\mathcal{G}$ by a smoothed value $\bar{\mathcal{G}}$ in the descent process. This acts as a preconditioner which allows the use of much larger steps and ensures that each new shape in the optimization sequence remains smooth. To apply smoothing in the ξ_1 direction, the smoothed gradient $\bar{\mathcal{G}}$ may be calculated from a discrete approximation to

$$\bar{\mathcal{G}} - \frac{\partial}{\partial\xi_1}\theta\frac{\partial\bar{\mathcal{G}}}{\partial\xi_1} = \mathcal{G}, \quad \bar{\mathcal{G}} = 0 \text{ at end points},$$

where θ is the smoothing parameter. If the modification is applied on the surface $\xi_2 =$ constant, then the first order change in the cost function is

$$\delta I = -\int\int \mathcal{G}\delta\mathcal{F}\,\mathrm{d}\xi_1 = -\lambda\int\int\left(\bar{\mathcal{G}} - \frac{\partial}{\partial\xi_1}\theta\frac{\partial}{\partial\xi_1}\bar{\mathcal{G}}\right)\bar{\mathcal{G}}\,\mathrm{d}\xi_1$$

$$= -\lambda\int\int \bar{\mathcal{G}}^2 + \theta\left(\frac{\partial\bar{\mathcal{G}}}{\partial\xi_1}\right)^2\mathrm{d}\xi_1 < 0,$$

again guaranteeing an improvement unless $\bar{\mathcal{G}} = \mathcal{G} = 0$ and assuring an improvement if λ is sufficiently small and positive.

In some problems, it turns out that the Hessian can be represented as a second order differential operator, so that with a proper choice of the smoothing parameter, the method becomes the Newton method. Search methods were intensively evaluated in a recent study by Jameson *et al.* (Jameson and Vassberg 1999) and it was verified that these sample problems (which may have a high linear content) could be solved with a number of search steps independent of the number of design variables.

7. Design process

The design process used in this work will change the shape of the wing in order to minimize its time-averaged coefficient of drag. The shape of the wing is constrained such that the maximum thickness to chord ratio remains constant between the initial and final designs. In addition, the mean angle of attack is allowed to vary to ensure the time-averaged coefficient of lift remains constant between designs.

The UFSYN88-MBC developed by Nadarajah and Jameson (2002) and Nadarajah (2003), employs a non-linear frequency domain method in the solution of the unsteady Euler equations. The NLFD adjoint based design procedure require the following steps:

1. *Periodic flow calculation at constant time averaged lift*. A set of multigrid cycles is used to drive the unsteady residual to a negligible value for all the modes used in the representation of the solution. In the case of a design process that constrains the time averaged lift, the mean angle of attack is perturbed every 10 multigrid cycles to maintain a constant time averaged coefficient of lift. This allows the unsteady residual to reduce by an order to two in magnitude before the angle is modified again.
2. *Adjoint calculation*. The adjoint equation is solved by integrating in reverse time. With minor modifications, the NLFD numerical scheme employed to solve the flow equations is used to solve the adjoint equations in reverse time.
3. *Gradient evaluation*. An integral over the last period of the adjoint solution is used to form the gradient. This gradient is then smoothed using an implicit smoothing technique. This ensures that each new shape in the optimization sequence remains smooth and acts as a preconditioner which allows the use of much larger steps. The smoothing leads to a large reduction in the number of design iterations needed for convergence. Refer to Nadarajah and Jameson (2002) for a more comprehensive overview of the gradient smoothing technique. An assessment of alternative search methods for a model problem is given by Jameson and Vassberg (1999).
4. *Wing shape modification*. The wing shape is then modified in the direction of improvement using the smoothed steepest descent method described in the previous section.
5. *Grid modification*. The internal grid is modified based on perturbations on the surface of the wing. The method modifies, the grid points along each grid index line projecting from the surface. The arc length between the surface point and the far-field point along the grid line is first computed, then the grid point at each location along the grid line is attenuated proportional to the ratio of its arc length distance from the surface point and the total arc length between the surface and the far-field.
6. *Repeat the design process*. The entire design process is repeated until the objective function converges. The problems in this work typically required between 9 and 40 design cycles to reach the optimum.

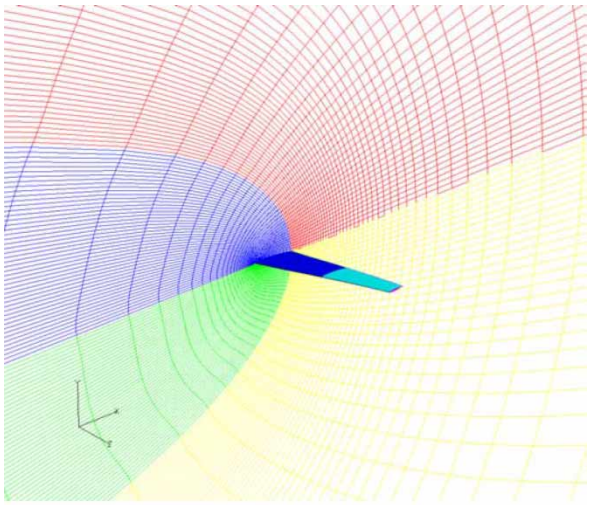

(a) Block Structure

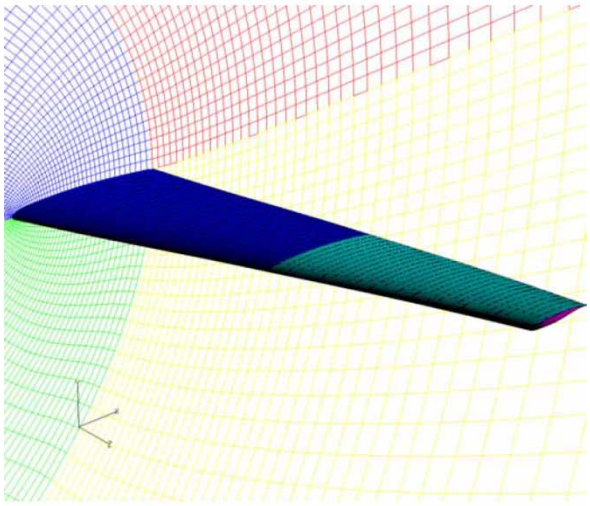

(b) Close-up View

Figure 3. LANN wing grid block structure; domain topology, $N_{p_i} = 4$, $N_{p_j} = 1$, $N_{p_k} = 3$; and grid size, $n_x \times n_j \times n_k = 193 \times 33 \times 97$.

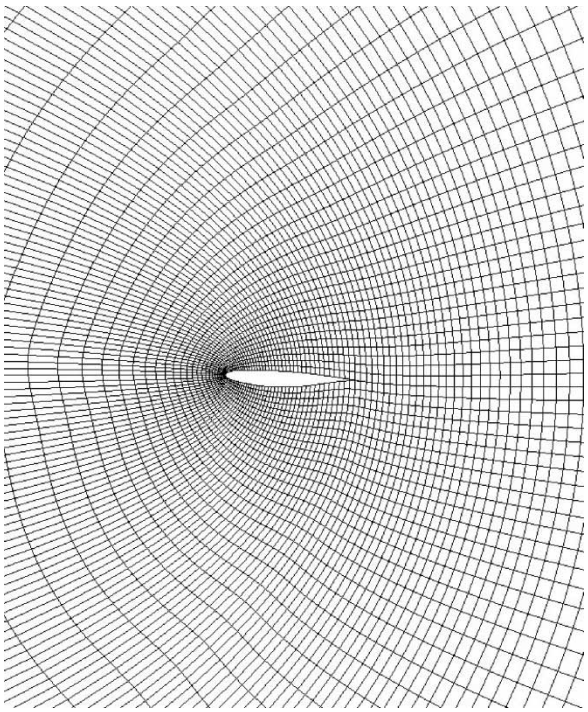

(a) Close-up View of Wing Root

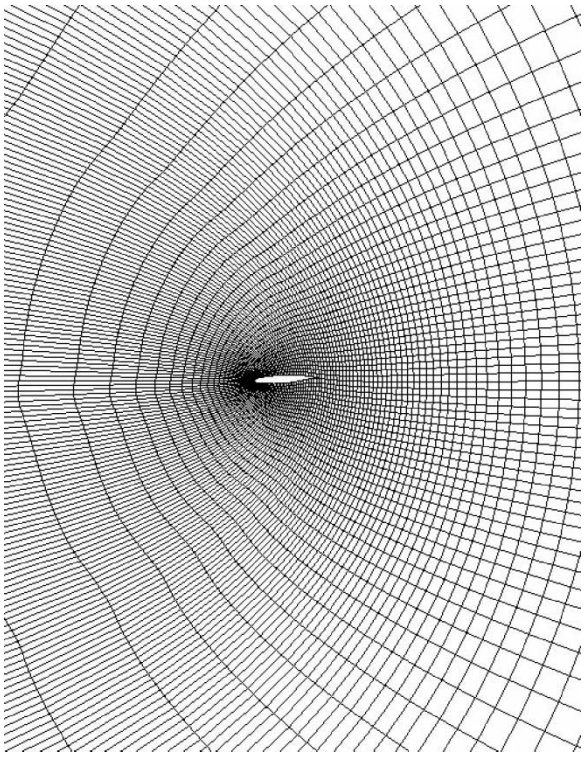

(b) Close-up View of Wing Tip

Figure 4. LANN wing mesh; grid size $n_x \times n_j \times n_k = 193 \times 33 \times 97$.

8. Results

The following subsections presents results from simulations of a three-dimensional wing undergoing a change in angle of attack as a function of time.

$$\alpha(t) = \alpha_{\mathrm{o}} + \alpha_{\mathrm{m}} \sin(\omega t).$$

For the cases presented in this section, the mean angle of attack, α_{o} is 0.59° for the validation case and 0° for the design test cases. For both cases, the deflection angle, α_{m} is set to ±0.25°. The reduced frequency, $\omega c/2V_\infty$, is set to 0.102, with a far-field Mach number, M_∞, of 0.82. The wing is pitched about the 61.2% of the root chord. The flight conditions are based on *Run 73* of the central transonic test case CT5 conducted by Zwaan (1985) at the NLR.

The first part of the results section contains a code validation study. The NLFD flow and adjoint solver convergence are presented. Surface pressure distributions are compared to both experimental data and other numerical simulations. The pressure distributions are also compared between the time accurate and NLFD methods. In the second section, a redesign of the LANN wing is demonstrated. Lastly, a gradient comparison between various number of temporal modes is presented.

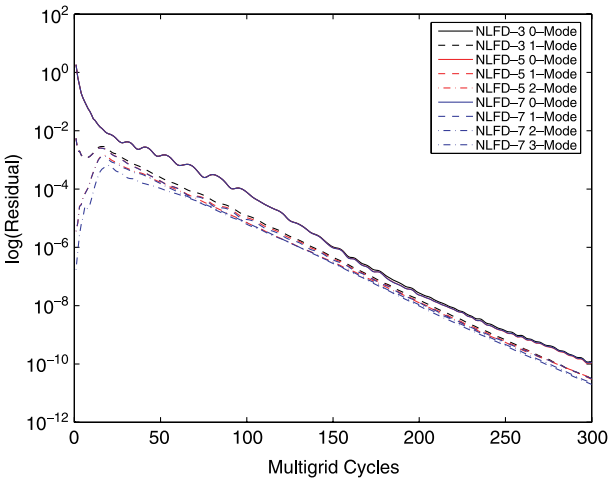

Figure 5. NLFD flow solver convergence; $M_\infty = 0.82$, $\omega_r = 0.102$.

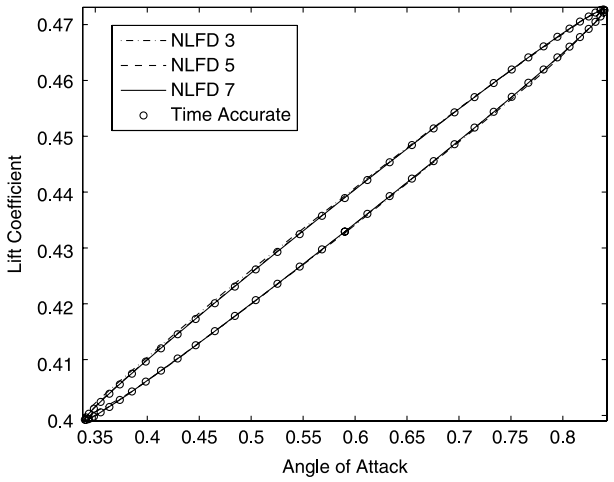

Figure 7. Comparison of lift hysteresis for various modes; $M_\infty = 0.82$, $\omega_r = 0.102$.

8.1 Validation

The computational grid employed for the validation study is a block structured grid as illustrated in figure 3. The block domain topology is based on a $N_{p_i} = 4$, $N_{p_j} = 1$, $N_{p_k} = 3$, where N_p is the number of blocks in each direction. In this work, four blocks are used in the i direction, one in the j direction and three in the k direction as illustrated in figure 3(a). Each block contains a grid of size $n_x \times n_j \times n_k = 49 \times 33 \times 33$. The total grid is $193 \times 33 \times 97$. A cross-sectional view of the grid is shown in figure 4.

Figures 5 and 6 illustrate the convergence of the NLFD flow and adjoint solvers. Here, as designated in the legend, "NLFD-3 0-Mode" indicates the zeroth mode based on a temporal discretization of three time steps per period. The convergence was obtained for the LANN wing test case for three, five, and seven time steps per period. The zeroth mode for all cases converge at the same rate. The same is true for the first, second, and third modes. The flow solver attains machine zero accuracy within 500 multigrid cycles. The rate of convergence is smaller for the adjoint solver.

The lift hysteresis is demonstrated in figure 7 for various number of modes. As the wing oscillates at a small angle of attack, the shock wave moves back and forth about a mean location and is closely sinusoidal and lags the wing motion. This lag is evident in the lift hysteresis loop where the maximum lift does not occur at the maximum angle of attack. The non-linear behavior of unsteady transonic flows is primarily due to the movement of the shock and this is evident in figure 7. Figure 7 describes that one harmonic is sufficient to produce an accurate lift hysteresis. However, figure 8 demonstrates that at least two harmonics are needed to capture the variation of the drag coefficient vs. angle of attack accurately; nevertheless, the difference is very small. Figure 9 demonstrates the variation of lift vs. drag coefficient, further providing evidence that at least two harmonics are required to accurately capture the flow field

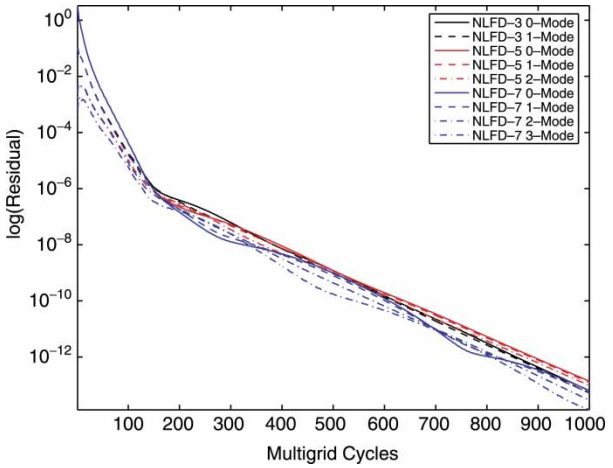

Figure 6. NLFD adjoint solver convergence; $M_\infty = 0.82$, $\omega_r = 0.102$.

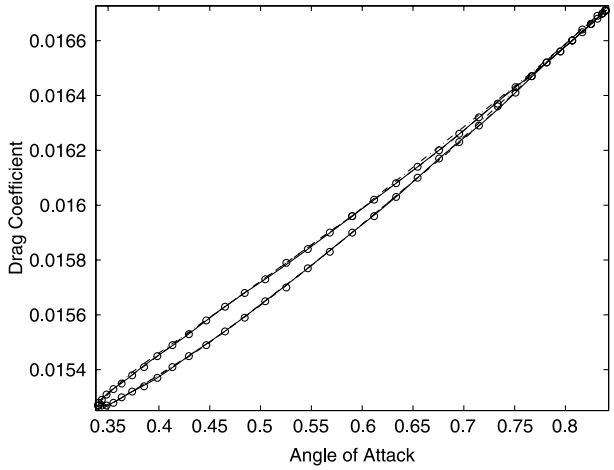

Figure 8. Comparison of drag coefficient vs. angle of attack for various modes; $M_\infty = 0.82$, $\omega_r = 0.102$.

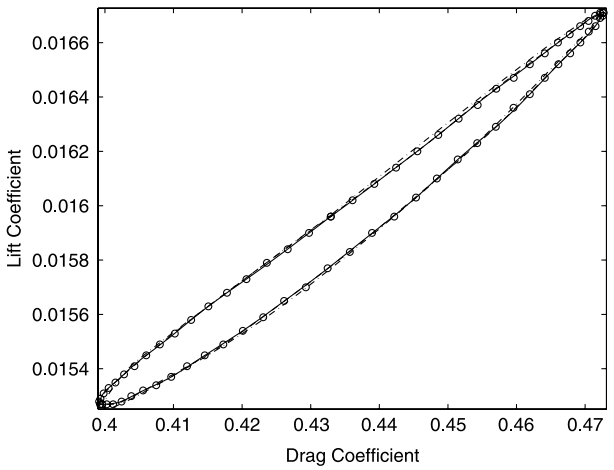

Figure 9. Comparison of lift vs. drag coefficient for various modes; $M_\infty = 0.82$, $\omega_r = 0.102$.

for the LANN wing, *Run 73*. Since this discrepancy is negligible, the three time step per period case is sufficient.

In figures 10 and 11, a validation of the surface pressure coefficients are presented. Figure 10 illustrates the pressure distribution for two different angles of attacks at two separate span stations. In figure 10(a) results based on the NLFD method are compared to experimental data and viscous solutions obtained by Gopinath and Jameson (2005) at the span location, $\eta = 20\%$ and angle of attack, $\alpha = 0.59°$. Note that "NLFD 11" indicates the solution was acquired with 11 time steps per period using the NLFD method. The inviscid NLFD results compare closely with Gopinath's viscous solutions, however, the location of the shock for the inviscid NLFD solution differs by 5% of the chord. This is an expected result, since the location of the shock is generally dependent on viscous effects especially for unsteady flows. The work in this paper focused on inviscid flows since the primary goal was to develop and implement the three-dimensional NLFD adjoint algorithms. Viscous terms are currently being implemented. Nevertheless, both solutions differ from the experimental work and further research is necessary to investigate the discrepancy. One possible reason for the difference could be due to the effect of the turbulence model on the unsteady viscous flows. Figures 10(b)–(d) illustrate the comparison at the maximum angle of attack

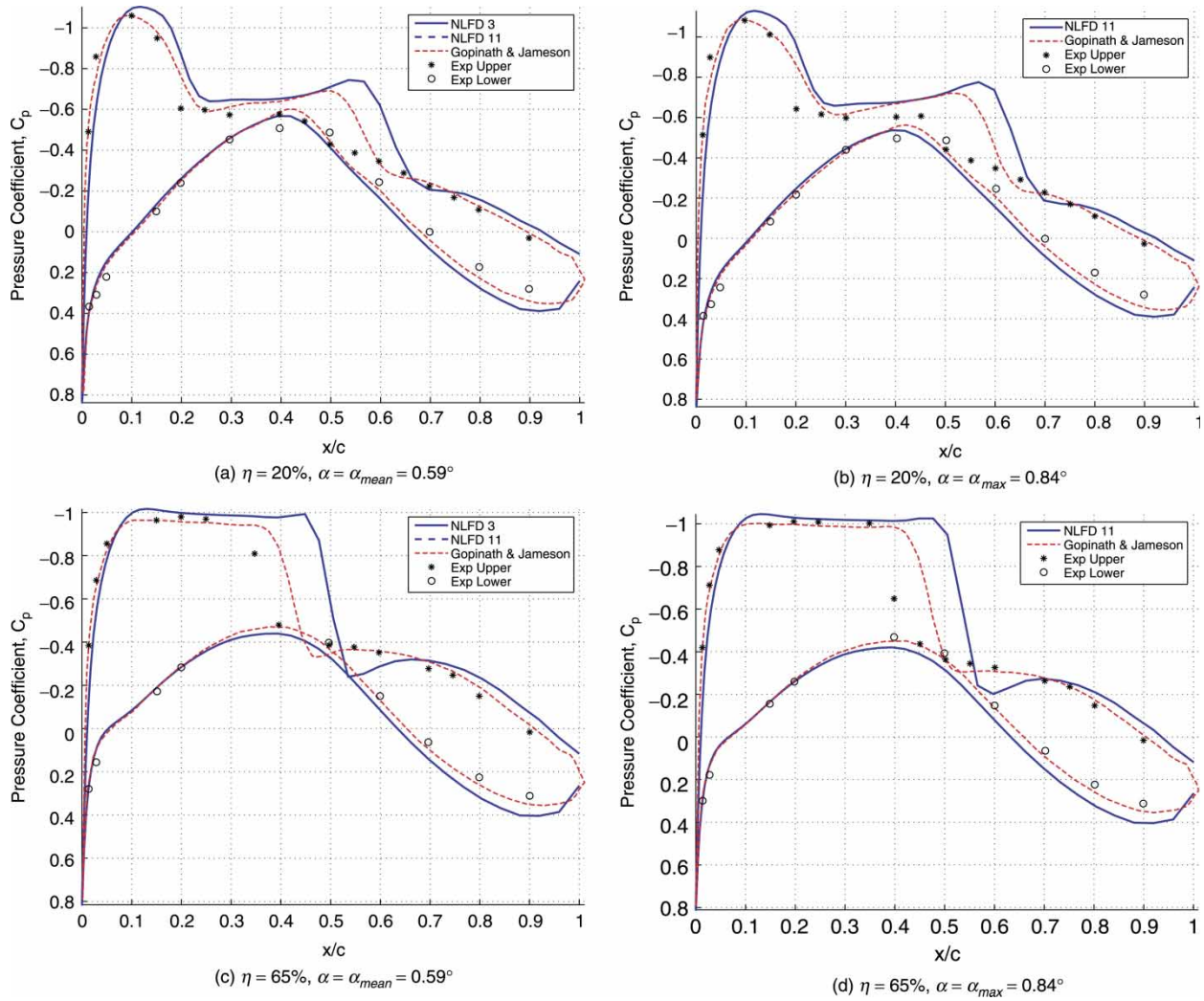

Figure 10. Comparison of pressure distribution with experimental data for the LANN wing, run 73, $M_\infty = 0.82$, $\omega_r = 0.102$.

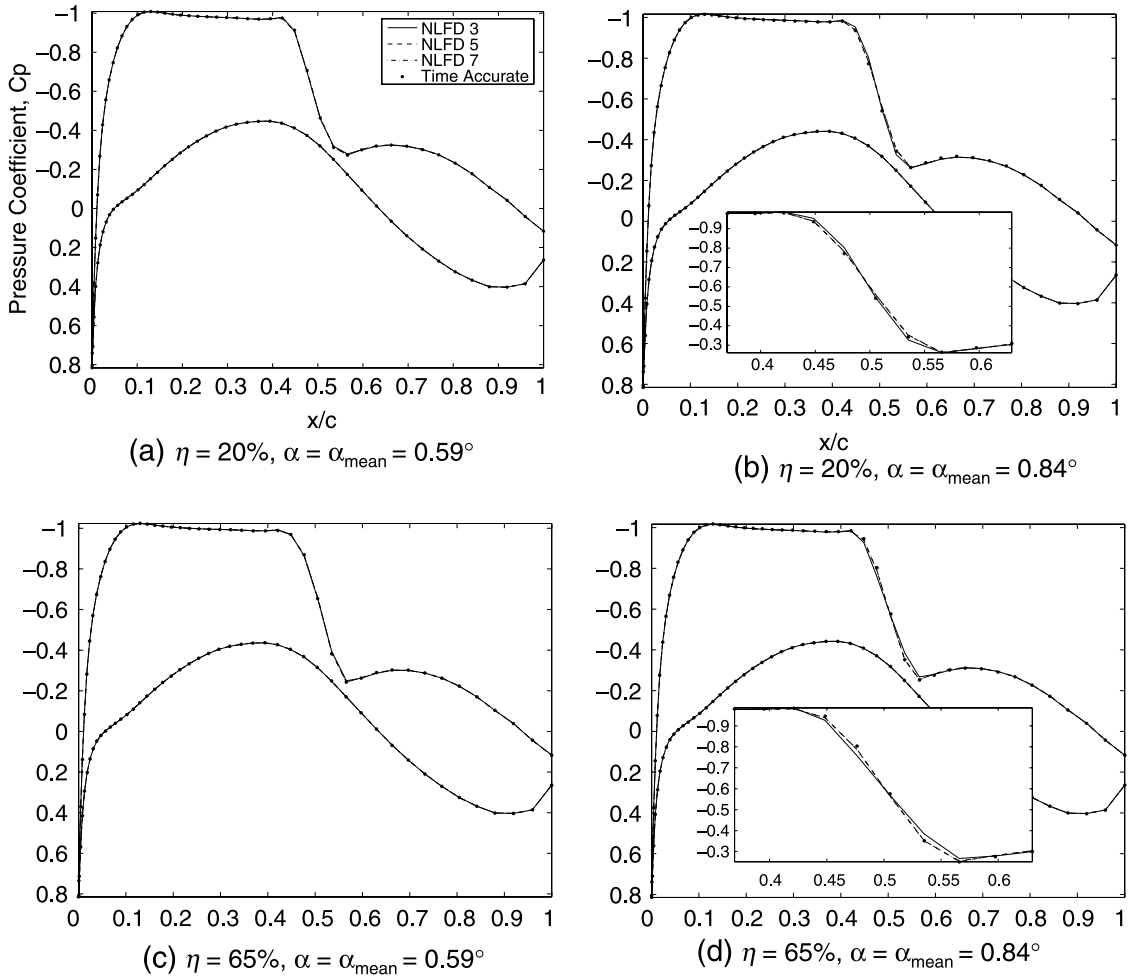

Figure 11. Comparison of pressure distribution for various time accurate and NLFD solutions at the 65% span station for the LANN wing, run 73; $M_\infty = 0.82$, $\omega_r = 0.102$.

and at a different span location. Similar trends are observed for these conditions.

A comparison between the time accurate and NLFD method is presented in figure 11. Here various time steps for both the time accurate and NLFD methods are illustrated. The figures show a nearly perfect match between the two methods. The time accurate solutions were obtained for temporal resolutions with 12, 24, 36, and 72 time steps per period. The case with 24 time steps per period are illustrated in figure 11. The solutions were obtained with 20 multigrid cycles per time step and five periods, which was necessary to ensure that the transient solutions were sufficiently eliminated before a periodic steady state solution was acquired. The NLFD solutions were obtained with 100 multigrid cycles for each mode. The figures illustrate that with three time steps per period, the NLFD method is able to capture identical results. Similar gains were observed by McMullen (2003) and Gopinath (Gopinath and Jameson 2005). In figure 11(b) and (d), a close-up view of the pressure distribution across the shock is illustrated. The figure shows a slight deviation of the NLFD case with three time steps per period from the time accurate and NLFD solutions with both five and seven time steps. This deviation is very small, yet it is the source of the discrepancy seen in figure 8. To further validate the NLFD approach for three-dimensional unsteady flows, figure 12 demonstrates the pressure distribution for various NLFD and time accurate solutions at span stations 3.1, 20, 45.3 and 95.3%. At each span station, the figure shows the comparisons at the 0, 90 and 270° phases. The figures show that with just three time steps per period, the three-dimensional unsteady flow over the entire wing is well represented. The time accurate solution in the figure is based on 24 time steps per period.

An investigation of the real and imaginary components of the first mode of the pressure coefficient is explored in figure 13. The cases with five and seven time steps provide approximately identical solutions, but the real component of the three time step case is vastly distinct. We believe this difference is the source of the dissimilarity seen in the pressure distribution at the shock as shown in figure 11(b) and that of the variation of the drag coefficient illustrated in figure 8. However, the small magnitude of the real component of the first mode provides an insignificant contribution to the total pressure distribution and the differences in figures 8 and 11(b) are negligible and does not warrant the need for a temporal resolution of five time

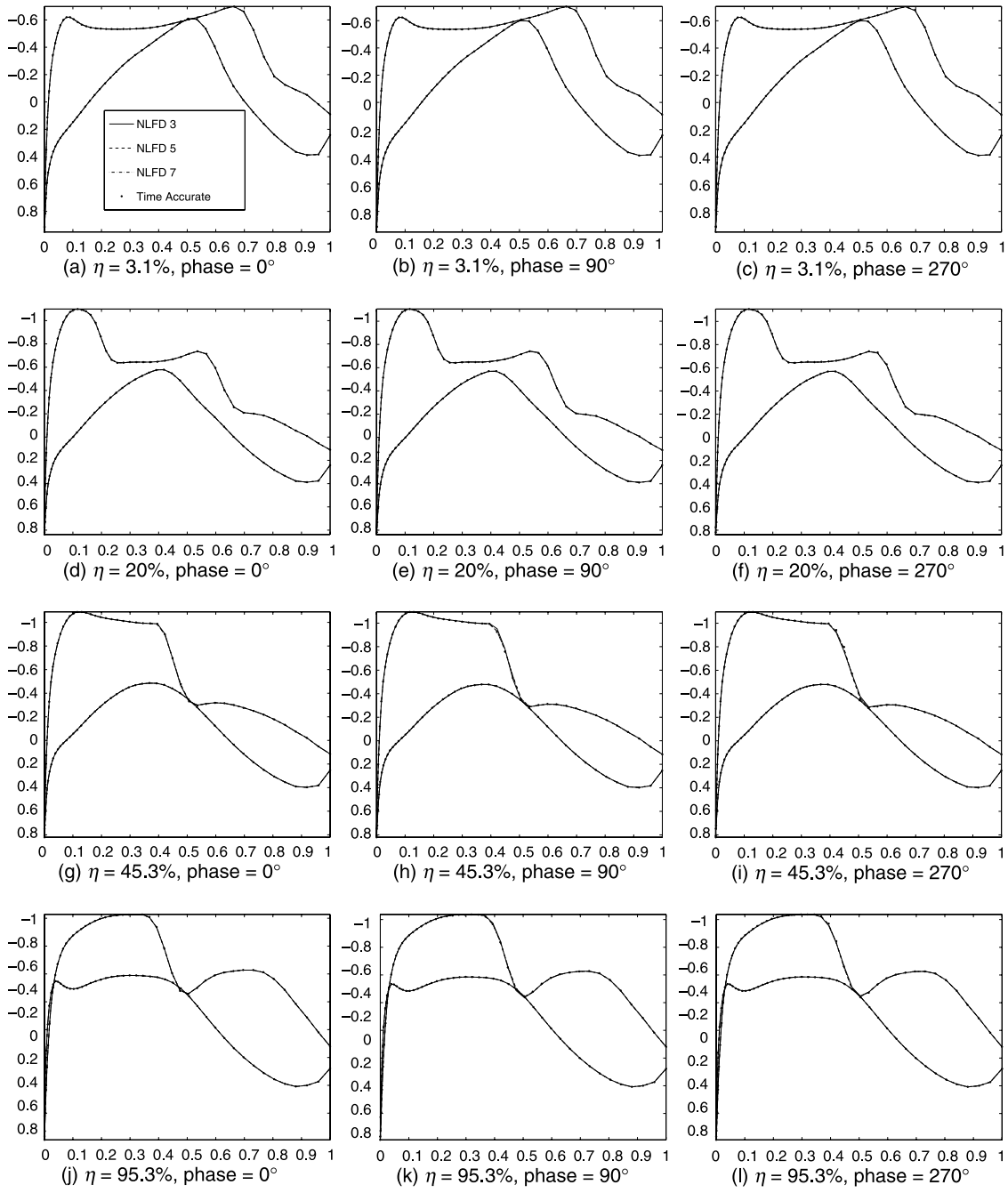

Figure 12. Comparison of pressure distribution for various time accurate and NLFD solutions for the LANN wing, run 73, $M_\infty = 0.82$, $\omega_r = 0.102$.

steps per period. Therefore, three time steps per period is sufficient and will be employed in the redesign of the LANN wing.

8.2. LANN wing: redesign

This section documents the results of the redesign of the LANN wing to reduce the time-averaged drag coefficient for a fixed time-averaged lift coefficient and wing thickness ratio. The simulation was performed at a Mach number, $M_\infty = 0.82$, reduced frequency, $\omega_r = 0.102$ and deflection of $\pm 0.25°$ about the zero angle of attack. During the initial stage to compute the flow solution, the time-averaged lift and drag are computed and used as the target lift and objective function. During the subsequent design cycles, the mean angle of attack is modified at each multigrid cycle to maintain the time-averaged lift coefficient. About 10 multigrid cycles are used for both the flow and adjoint solvers per design cycle.

Figures 14–16 illustrate the wing surface pressure contour and the initial and final pressure distributions at three span locations for each time step after 38 design cycles. The first time step corresponds to phase = 0°, the second to phase = 120°, and the third to phase = 240°. In figure 14, the pressure contour illustrates the absences

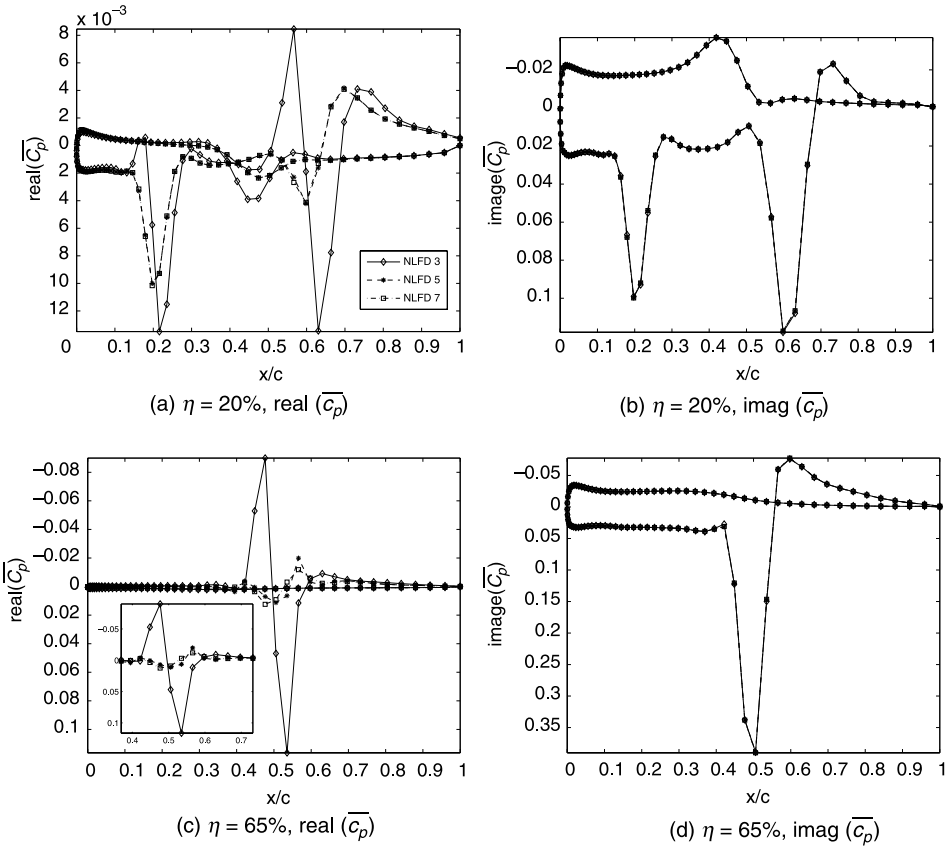

Figure 13. Comparison of the real and imaginary components of the first harmonic pressure coefficient for various modes and span stations; $M_\infty = 0.82$, $\omega_r = 0.102$. (a) $\eta = 20\%$, real($\overline{c_p}$); (b) $\eta = 20\%$, imag($\overline{c_p}$); (c) $\eta = 65\%$, real($\overline{c_p}$); and (d) $\eta = 65\%$, imag($\overline{c_p}$).

of a shock wave and this is further validated in the three pressure coefficient plots at span stations 6.2, 49.2 and 92.3%. The initial pressure distribution is illustrated as a dotted line, while the solid is at the final design. The plots show an elimination of the shock wave at the mid-section with a reduction of the sectional drag coefficient from 0.0037 to 0.0030. The mean angle of attack was perturbed from the initial zero degrees to $-0.105°$ to maintain the time-averaged lift coefficient at 0.3483. The time-averaged drag coefficient reduced by 10.5% from 0.01168 to 0.01045 within 38 design cycles. The design is halted once the change in the objective function or time-averaged drag coefficient reaches a level of $1{\cdot}E-8$. The figure also demonstrates the initial and final, illustrated by a dotted and solid line, cross-sectional airfoil profiles. A distinctive feature of the new airfoil is the reduction of the upper surface curvature. The reduced curvature contributes to the elimination of the shock wave in the mid-section region of the LANN wing. At the 120 and 240° phases, as illustrated in figures 15 and 16, a severe weakening of the shock wave in the mid and tip sections of the LANN wing are observed. At the 120° phase, the mid-section sectional drag coefficient decreased from 0.0053 to 0.0043.

In figures 17 and 18, the initial and final surface pressure distributions are shown at the 0 and 120° phases. The weakening of the λ-shock system is demonstrated

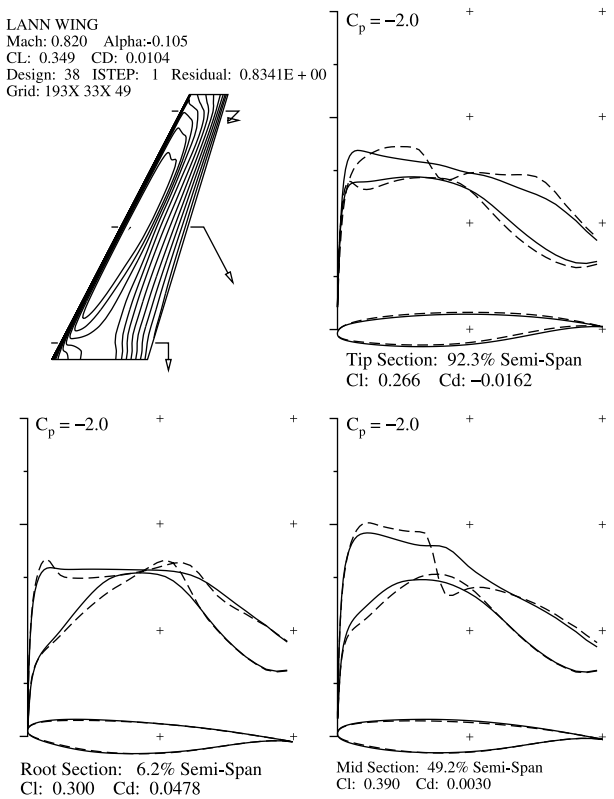

Figure 14. Initial and final pressure distribution for various span locations at phase = 0°.

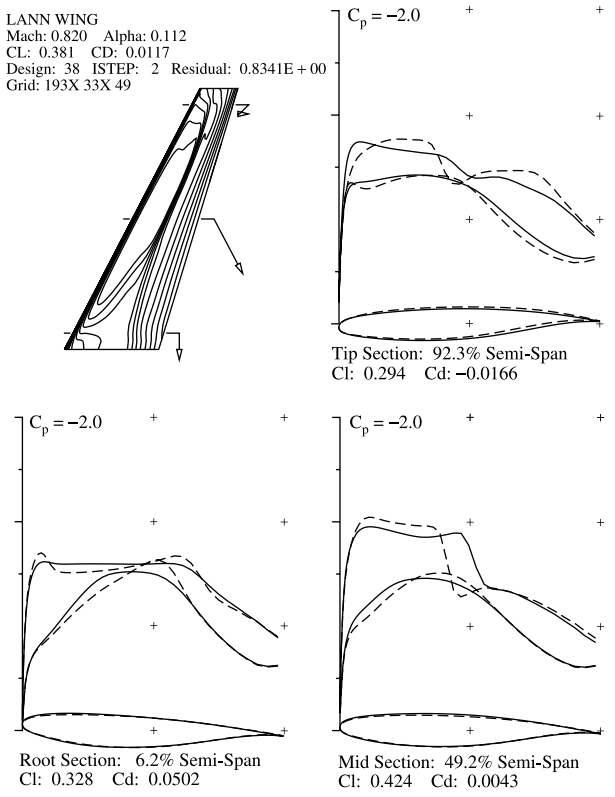

Figure 15. Initial and final pressure distribution for various span locations at phase = 120°.

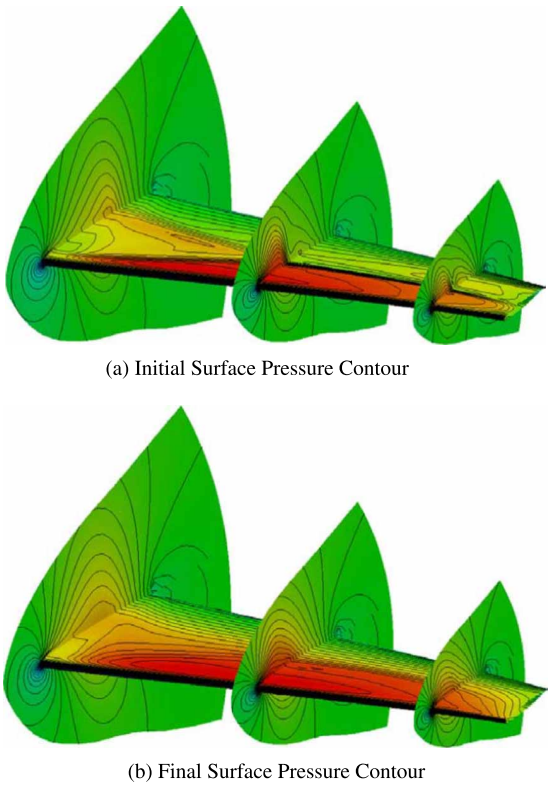

(a) Initial Surface Pressure Contour

(b) Final Surface Pressure Contour

Figure 17. (a) Initial and (b) final surface pressure contours at 0° Phase for the LANN wing, run 73, $M_\infty = 0.82$, $\omega_r = 0.102$.

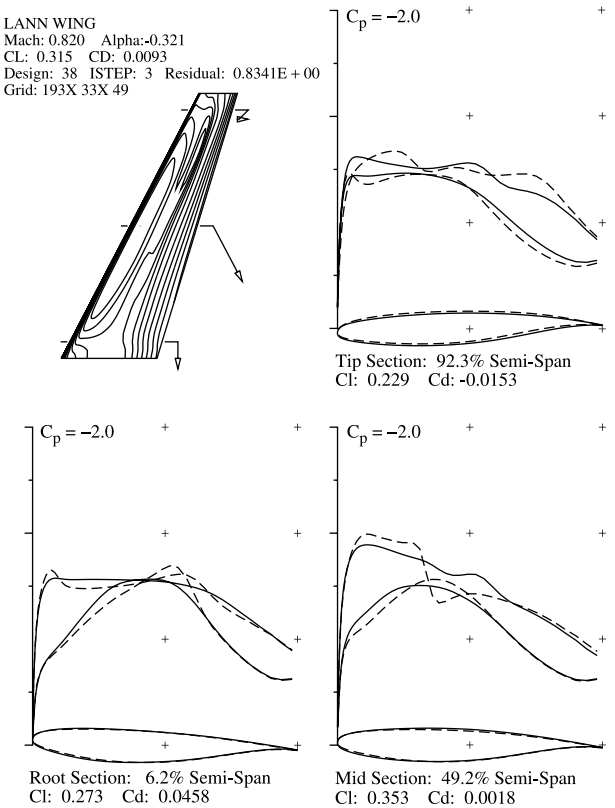

Figure 16. Initial and final pressure distribution for various span locations at phase = 240°.

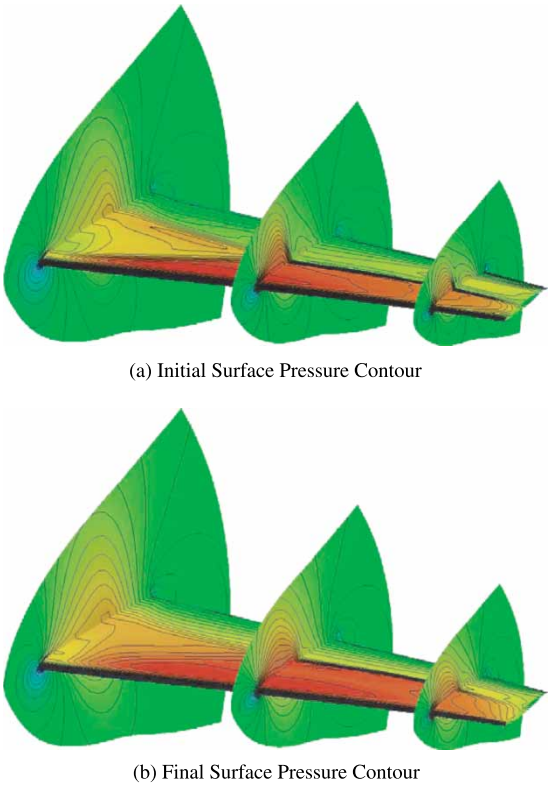

(a) Initial Surface Pressure Contour

(b) Final Surface Pressure Contour

Figure 18. (a) Initial and (b) final surface pressure contours at 120° Phase for the LANN wing, run 73, $M_\infty = 0.82$, $\omega_r = 0.102$.

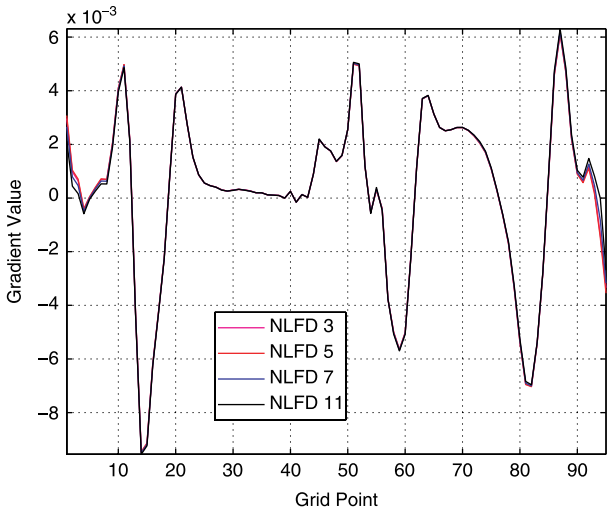

Figure 19. Comparison of gradient for various time steps per period at $\eta = 5\%$.

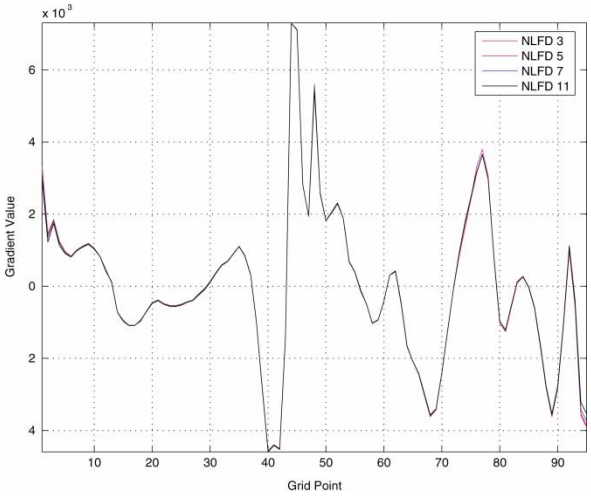

Figure 21. Comparison of gradient for various time steps per period at $\eta = 92\%$.

in figure 18(b). A complete elimination of the shock is observed at the 0° phase.

The Validation section illustrated the ability of the NLFD method to accurately model the flow with only three time steps per period. However, for the case of optimum shape design, the accuracy of the gradient of the objective function is of paramount importance. Figures 19–21 illustrate the gradients of the objective function at three different span locations for various temporal modes. The gradients are plotted in a clockwise direction starting from the lower trailing edge to the leading edge and ending at the upper trailing edge point. The figures illustrate that with just three time steps per period, the gradients can be accurately captured. Lastly, figure 22 presents the convergence of ΔI, where I is the objective function (time-averaged drag coefficient). ΔI converges linearly as expected. Linear convergence is characteristic of a steepest descent type method. The code is automatically stopped as soon as a change of 1·E − 8 is detected. This level of change corresponds to a change to the eighth decimal place of the drag coefficient and this is sufficient for engineering accuracy.

9. Conclusion

The NLFD method produce essentially identical results with just three time steps per period when compared to the time accurate method. A redesign of the LANN wing has been demonstrated with a reduction of the time-averaged drag coefficient by 10.5% while maintaining the time-averaged lift coefficient. The NLFD method with just three time steps per period also provides accurate gradients. These results further demonstrate the potential of the method to provide significant improvements to more realistic problems such as helicopter rotors, turbomachinery and other unsteady devices operating in the transonic regime.

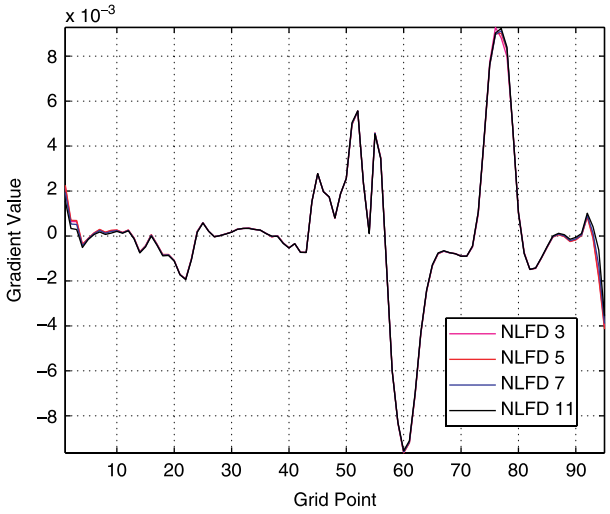

Figure 20. Comparison of gradient for various time steps per period at $\eta = 49\%$.

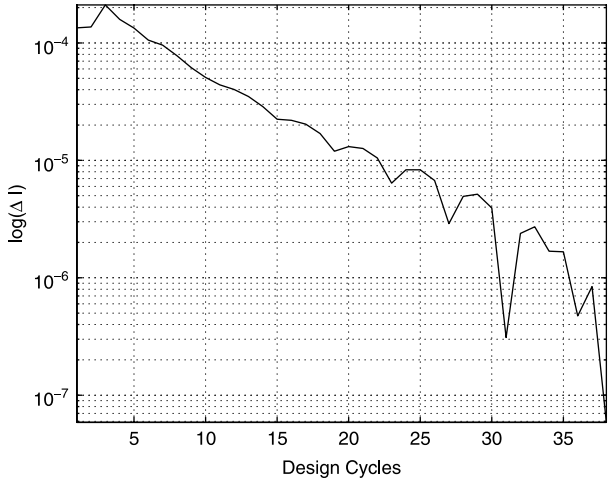

Figure 22. Convergence of ΔI, where I is the time-averaged drag coefficient.

References

Adamczyk, J.J., Model equation for simulating flows in multistage turbomachinery. Technical report, NASA Technical Memorandum 86869, November 1984.

Davis, R., Personal communications on TFLO, January–December 2001.

Duta, M.C., Giles, M.B. and Campobasso, M.S., The harmonic adjoint approach to unsteady turbomachinery design. *Int. J. Numer. Meth. Fluids*, October 2002, **40**, 323–332.

Gopinath, A.K. and Jameson, A., Time spectoral method for periodic unsteady computations over two- and three- dimensional bodies. *AIAA Paper 2005-1220*, January 2005 (43rd Aerospace Sciences Meething and Exhibit: Reno, NV).

Hall, K.C., Seminar on harmonic balance techniques. Technical report, Presented to the Aerospace Computing Lab, Stanford University, 2000.

Hall, K.C., Thomas, J.P. and Clark, W.S., Computation of unsteady nonlinear flows in cascades using a harmonic balance technique. Technical report, 9th International Symposium on Unsteady Aerodynamics, Aeroacoustics and Aeroelasticity of Turbomachines, Lyon, France, September, 2000.

Jameson, A., Computational aerodynamics for aircraft design. *Science*, 1989, **245**, 361–371.

Jameson, A., Time dependent calculations using multigrid, with applications to unsteady flows past airfoils and wings. *AIAA Paper 91-1596*, June 1991 (AIAA 10th Computational Fluid Dynamics Conference: Honolulu, Hawaii).

Jameson, A., Optimum aerodynamic design using CFD and control theory. *AIAA paper 95-1729*, June 1995 (AIAA 12th Computational Fluid Dynamics Conference: San Diego, CA).

Jameson, A. and Vassberg, J.C., Studies of alternative numerical optimization methods applied to the brachistochrone problem. *OptiCON 99*, 1999.

Jameson, A., Schmidt, W. and Turkel, E., Numerical solutions of the Euler equations by finite volume methods with Runge-Kutta time stepping schemes. *AIAA Paper 81-1259*, January 1981.

McMullen, M., *The Application of Non-Linear Frequency Domain Methods to the Euler and Navier-Stokes Equations*, PhD dissertation, Department of Aeronautics and Astronautics, Stanford University, Stanford, CA, March, 2003.

McMullen, M., Jameson, A. and Alonso, A., Acceleration of convergence to a periodic steady state in turbomachinery flows. *AIAA Paper 01-0152*, 2001 (39th Aerospace Sciences Meeting and Exhibit: Reno, NV).

McMullen, M., Jameson, A. and Alonso, A., Application of a non-linear frequency domain solver to the Euler and Navier-Stokes equations. *AIAA Paper 02-0120*, Jan 2002 (40th Aerospace Sciences Meeting and Exhibit: Reno, NV).

Nadarajah, S., *The Discrete Adjoint Approach to Aerodynamic Shape Optimization*, PhD dissertation, Department of Aeronautics and Astronautics, Stanford University, Stanford, CA, January 2003.

Nadarajah, S. and Jameson, A., A comparison of the continuous and discrete adjoint approach to automatic aerodynamic optimization. *AIAA Paper 2000-0667*, January 2000 (38th Aerospace Sciences Meeting and Exhibit: Reno, Nevada).

Nadarajah, S. and Jameson, A., Studies of the continuous and discrete adjoint approaches to viscous automatic aerodynamic shape optimization. *AIAA Paper 2001-2530*, June 2001 (15th Computational Fluid Dynamics Conference: Anaheim, CA).

Nadarajah, S. and Jameson, A., Optimal control of unsteady flows using a time accurate method. *AIAA Paper 2002-5436*, September 2002 (9th AIAA/ISSMO Symposium on Multidisciplinary Analysis and Optimization Conference: Atlanta, GA).

Nadarajah, S., Jameson, A. and Alonso, J.J., Sonic boom reduction using an adjoint method for wing-body configurations in supersonic flow. *AIAA Paper 2002-5547*, September 2002 (9th AIAA/ISSMO Symposium on Multidisciplinary Analysis and Optimization Conference: Atlanta, GA).

Nadarajah, S., McMullen, M. and Jameson, A., Optimum shape design for unsteady flows using time accurate and non-linear frequency domain methods. *AIAA Paper 2003-3875*, June 2003 (16th. Computational Fluid Dynamics Conference: Orlando, FL).

Reuther, J., Alonso, J.J., Rimlinger, M.J. and Jameson, A., Aerodynamic shape optimization of supersonic aircraft configurations via an adjoint formulation on parallel computers. *AIAA Paper 96-4045*, September 1996 (6th AIAA/NASA/ISSMO Symposium on Multidisciplinary Analysis and Optimization: Bellevue, WA).

Reuther, J., Jameson, A., Farmer, J., Martinelli, L. and Saunders, D., Aerodynamic shape optimization of complex aircraft configurations via an adjoint formulation. *AIAA Paper 96-0094*, January 1996 (34th Aerospace Sciences Meeting and Exhibit: Reno, Nevada).

Snider, A., An improved estimate of the accuracy of trigonometric interpolation. *SIAM J. Numer. Anal.*, 1972, **9**(3), 505–508.

Thomas, J.P., Hall, K.C. and Dowell, E.H., A discrete adjoint approach for modelling unsteady aerodynamic design sensitivities. *AIAA Paper 03-0041*, Jan 2003 (41th Aerospace Sciences Meething and Exhibit: Reno, NV).

Zwaan, R.J., Data set 9, LANN wing. Pitching oscillation, Technical report. Agard-R-702 Addendum no. 1, AGARD, Amsterdam, Netherlands, 1985.